ELSEVIER

Contents lists available at ScienceDirect

Applied Surface Science

journal homepage: www.elsevier.com/locate/apsusc



Full Length Article



Structure and magnetism of ultra-small cobalt particles assembled at titania surfaces by ion beam synthesis

Abdulhakim Bake ^{a,b}, Md Rezoanur Rahman ^a, Peter J. Evans ^c, Michael Cortie ^d, Mitchell Nancarrow ^b, Radu Abrudan ^e, Florin Radu ^e, Yury Khaydukov ^f, Grace Causer ^a, Sara Callori ^g, Karen L. Livesey ^h, David Mitchell ^b, Zeljko Pastuovic ^c, Xiaolin Wang ^a, David Cortie ^{a,c,*}

- ^a Institute for Superconducting and Electronic Materials, University of Wollongong, NSW 2519, Australia
- ^b Electron Microscopy Centre, Innovation Campus, University of Wollongong, Wollongong, NSW 2519, Australia
- ^c The Australian Nuclear Science and Technology Organisation, Lucas Heights, NSW 2232, Australia
- d School of Mathematical and Physical Sciences, Faculty of Science, University of Technology Sydney, Ultimo 2007, Australia
- ^e BESSY, Hahn-Meitner-Platz 1, D-14109 Berlin, Germany
- f Max Planck Society, Outstation at the MLZ, 85748 Garching Germany/Max Planck Institute für Festkörperforschung, Stuttgart, 70569 Germany
- g Department of Physics, California State University, San Bernardino, CA, United States
- ^h The University of Newcastle, School of Mathematical and Physical Sciences, Newcastle, NSW 2308, Australia

ABSTRACT

Metallic cobalt nanoparticles offer attractive magnetic properties but are vulnerable to oxidation, which suppresses their magnetization. In this article, we report the use of ion beam synthesis to produce ultra-small, oxidation-resistant, cobalt nanoparticles embedded within substoichiometric $TiO_{2.\delta}$ thin films. Using high fluence implantation of cobalt at 20–60 keV, the particles were assembled with an average size of 1.5 ± 1 nm. The geometry and structure of the nanoparticles were studied using scanning transmission electron microscopy. Near-edge X-ray fluorescence spectroscopy on the $L_{2,3}$ Co edges confirms that the majority of the particles beneath the surface are metallic, unoxidised cobalt. Further evidence of the metallic nature of the small particles is provided via their high magnetization and superparamagnetic response between 3 and 300 K with a low blocking temperature of 4.5 K. The magnetic properties were studied using a combination of vibrating sample magnetometry, element-resolved X-ray magnetic circular dichroism, and depth-resolved polarised neutron reflectometry. These techniques provide a unified picture of the magnetic metallic Co particles. We argue, based on these experimental observations and thermodynamic calculations, that the cobalt is protected against oxidation beneath the surface of titania owing to the enthalpic stability of TiO_2 over CoO which inhibits solid state reactions.

1. Introduction

In nanotechnology, bigger is not better. The enduring quest to achieve smaller nanocrystals is motivated by the spectacular functionality that can occur once sizes approach the quantum regime. An example of this phenomenon is the design of cobalt nanomagnets as these exhibit large variations in their magnetization and spin anisotropy as a function of the cobalt particle size [1-2]. For nanomagnetic systems, cobalt is an intrinsically attractive member of the 3d-transition metals, as its properties excel in ultra-small structures, and can even rival or exceed those of iron, in special cases [1]. Atomic cobalt possesses the special $3d^7$ valence electronic configuration which theoretically hosts the largest possible total angular moment (J = L + S = 9/2), composed of the spin (S) and angular (L) contributions. This even exceeds the iron atomic moment $(3d^6, J = 4)$. In solids and nanocrystals, the magnetic moment

per atom is reduced by crystal-field effects, however the significant intrinsic spin contribution (S=3/2) of cobalt still gives a large magnetic moment that can be enhanced from 1.7 μ B in the bulk metal, to 2.3 μ B in small nanoclusters with 10–1000 atoms [1]. The effort to engineer cobalt into smaller structures with higher magnetic moments has a long history. Early work in the 1980s first showed that cobalt possessed magnetic order even in atomically-thin sheets, making it one of the first known examples of a 2D monolayer magnet [3–4]. Pioneering work showed that small metallic cobalt nanoclusters (with 10–300 atoms) have a magnetic moment that is enhanced by 20–30% over that of bulk cobalt [1]. An exciting development in the past decade was the realization that the angular momentum (L) of ultra-small cobalt magnets (>10 atoms) in low symmetry environments is not quenched, thus providing a net moment almost double the moment of bulk cobalt metal [2]. This was observed in combination with magnetic anisotropy that

E-mail address: dcortie@uow.edu.au (D. Cortie).

^{*} Corresponding author.

approaches the upper limit for any 3d transition metal [5]. Recently a large magnetic moment was also detected for cobalt clusters embedded in TiO2 suggesting it is possible to achieve enhanced moments for particles embedded in a 3D matrix [6-7]. These observations offer great promise for cobalt-nanomagnets in spintronic and other magnetic devices, that increasingly rely on magnetic materials as non-volatile storage elements, spin injectors, and sensors. Recent density functional theory (DFT) calculations show that the spin magnetic moment in cobalt clusters can exceed 2 μ_B for clusters consisting of 30 atoms, which correspond to particle diameters ~ 0.8 nm, and this also coincides with a metal-insulator transition [8]. However, to-date, the requirement for ultra-small cobalt particles has generally only been met using assembly in pristine surface environments. Table 1 in the Appendix compares the sizes of particles reported by different methods, showing standard chemical methods can generally only achieve cobalt particles larger > 3 nm, with a relatively large size distribution [8-30]. A separate unresolved issue is that, under real-world conditions, cobalt particle surfaces are vulnerable to ambient exposure and form rock-salt CoO phases, spinels and CoO/Co core-shells. This poses a major practical barrier and limits the down-scalability of cobalt nanomagnets as the oxide phases also have a detrimental effect on the magnetic properties since they are typically antiferromagnetic [31] and introduce a detectable magnetic unidirectional anisotropy (exchange bias) [32,33].

One potential avenue to synthesise *air-stable*, ultra-small cobalt ensembles is to use ion implantation to embed them in a passive host material, submerging them beneath the chemically-active surface. Ion beam synthesis (IBS) can be used to tune a wide range of material parameters at the nanoscale as illustrated in Fig. 1, and the beam-matter interaction can be exploited to assemble small particles by controlling the number (fluence) and speed (kinetic energy) of the incoming ions [34–35]. The advantage of using a particle beam method to implant ions, is that, fluence - the number of foreign ions incident on the target surface per unit area - can be tuned over a broad range. Adjusting this parameter, and the species of the incoming ion, allows the IBS technique to achieve a range of nanoarchitectures including: single-atom systems, traditional doping, substitution, sputtering, hyper-doping, self-assembly of clusters, and eventually the growth and coalescence of continuous

 Table 1

 Systematic literature review of the synthesis of Co nanoclusters.

Smallest Diameter Achieved (nm) avg.	Methodology	Ref.
$3.5\pm0.7~\mathrm{nm}$	microfluidic reactor synthesis	[57]
15–25 nm	Thermal decomposition ([bis(2-	[23]
	hydroxyacetophenato)cobalt(II)])	
2-4 nm	Microemulsion-mediated synthesis	[9]
35-200 nm	Modified polyol process	[16]
10 nm	Reduction of Co(NO ₃) ₂ in supercritical methanol	[26]
$5.13\pm0.65~\text{nm}$	Modified polyol process	[19]
$1.5\pm1~\text{nm}$	Ion implantation in SiO ₂	[14]
$3.5\pm1\;\text{nm}$	Ion exchange method	[20]
10-30 nm	Supercritical hydrothermal reduction process	[25]
15-60 nm	DC magnetron sputtering	[13]
25-35 nm	Thermal decomposition	[22]
2-4 nm	In situ from molecularly defined complex	[24]
$27.43\pm0.15~\text{nm}$	One step hydrothermal method	[11]
10.5 nm	One step solvothermal preparation	[17]
50–150 nm	Reduction of metallic ions absorbed into the	[21]
	hydrogel network	
9–14 nm	Thermal decomposition	[18]
20–60 nm	Methanol extract of Conocarpus erectus leaves as	[10]
	reducing agent	F077
20 nm	Ionization CVD	[27]
20–50 nm	Swift heavy ion irradiation	[12]
10–45 nm	Chemical reduction of [Co(NH ₃) ₅ ONO]Cl ₂ in alcoholic solution	[15]
20–30 nm	Anthracene mediated reduction of [CoCl ₄] ₂ – in potentiostatic electrolysis	[30]
0.5–2 um	Liquid phase reduction method	

layers (Fig. 1). By precisely controlling the nucleation of the dopant from the solid-solution, and offering the opportunity to operate at low temperatures where diffusion is limited, IBS can form extremely small clusters, and metastable defect configurations, that are not possible with standard chemical techniques. The growth and ripening mechanism for particles during the implantation process is also quite different from traditional thermally-driven Ostwald ripening. Indeed, the bombardment of incoming ions during the implantation process can potentially lead to fragmentation of the existing particles into smaller clusters, via the so-called inverse-Ostwald ripening process, in which smaller precipitate clusters grow at the expense of larger ones [36]. In this context, ion-beam implantation of cobalt in SiO2 has been heavily studied and the formation of ultra-small nanoclusters is well known [37-38]. Spherical cobalt particles ranging between 2 and 13 nm in SiO₂ have been reported in the past [37–38]. Although the small sizes achieved in past IBS work are attractive, the major issue identified from the latter implantation studies into SiO_2 is that a large fraction of the cobalt atoms are oxidised in the as-implanted state. Thus, to achieve metallic particles, a high-temperature reduction treatment is required. This hightemperature treatment, in general, leads to coarsening and growth of the particles via traditional Ostwald ripening, which then makes it difficult to retain the ultra-small particle size. To date, there also appears to be very little experimental information about the magnetic response of cobalt metal clusters formed using the novel IBS approach. Redox reactions are expected to modify the magnetic state of the cobalt atoms. The oxidation reactions that occur during the implantation depend on the intrinsic solid-state chemistry at play between the host matrix and the particle species. It is therefore advantageous to explore alternate chemistry to go beyond the heavily-explored Co:SiO2 combination and advance the frontier for ultra-small cobalt nanoclusters formed by IBS.

To this end, work on cobalt implantation into titania TiO2 has emerged as a promising, alternative pathway to assemble cobalt clusters that are quite robust against oxidation. This discovery, in large part, was an unexpected product of the widespread efforts to explore the intrinsic dilute magnetic oxide semiconducting (DMOS) behavior in $Co_xTi_{1-x}O_{2-\delta}$ [6]. Over the past decade, a large body of research identified that cobalt tends to self-assemble into stable metallic particles in a titania host. Early DFT studies showed it was energetically advantageous for two cobalt atoms to occupy neighboring substitutional sites in TiO₂ [39], which leads to a tendency for clustering and self-assembly. Numerous synthesis methods, including pulsed laser deposition, sol-gel, and magnetron sputtering, support the existence of metallic cobalt phase segregation in TiO₂. Compared to traditional methods, however, there is far less published work on the use of IBS to form cobalt nanomagnets in titania. Khaibullin et al. studied heavily implanted rutile crystals [40]. Akdogan et al. studied implantation of Co into rutile and reported a hightemperature ferromagnetic response [41]. Ding et al. studied the origin of ferromagnetism in Co-implanted rutile (110) single crystals, [42] and concluded that the major contribution to the ferromagnetism is due to formation of metallic Co nanocrystals. Studies of amorphous TiO2 matrices are more limited. Yildirim et al. reported that cobalt implanted into amorphous TiO2 yielded paramagnetic properties, which suggests that particles are not formed at the low fluences studied in that work [43]. However, at higher doses, there have been clear indications of metallic cobalt clusters forming, albeit with an unknown size distribution. For example, later work, performed by our group, found that cobalt implanted into amorphous TiO2 produced strong magnetic properties for high fluences, and X-ray photoemission spectroscopy (XPS) and reflectometry data suggested that the cobalt was in the metallic state [6]. Feature sizes between 1 and 4 nm were observed in the transmission electron microscopy (TEM) in the latter work, but it was not possible to directly image the atomic-scale details of single particles [6]. Therefore, although the latter studies strongly suggest that ultra-small cobalt nanoclusters can be formed in TiO2 using implantation above some threshold fluence, there has so far been no consensus on what the optimum conditions are to assemble ultra-small nanoparticles.

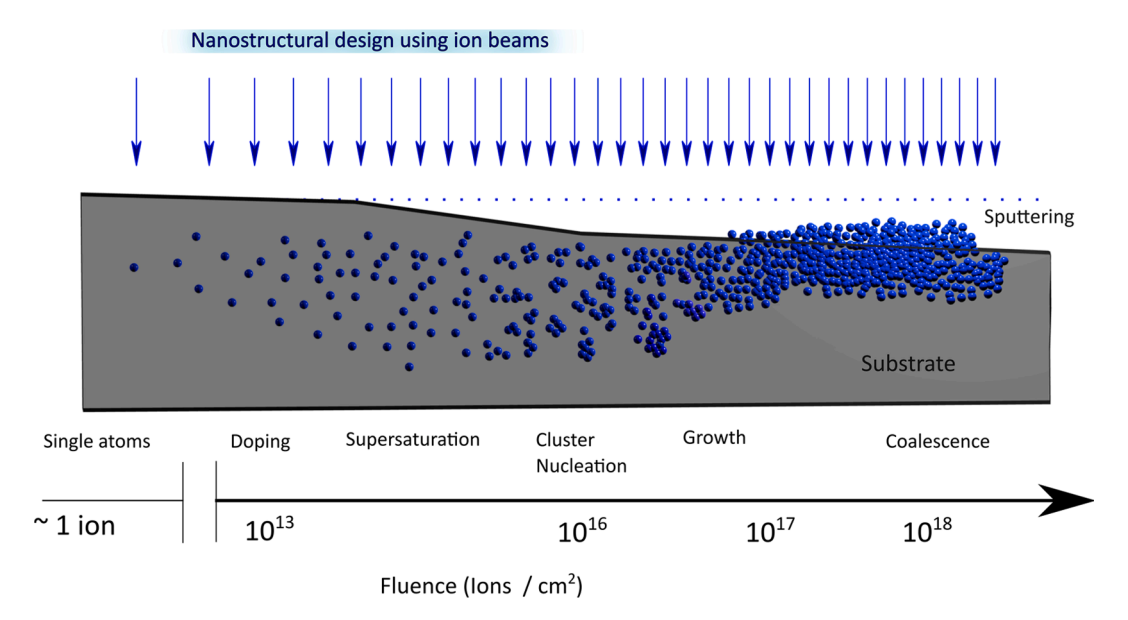


Fig. 1. (a) Schematic illustration of materials modification during ion beam synthesis. The fluences are approximate values, which will differ for different materials and ion beam species depending on the underlying chemical factors such as the solubility.

Furthermore, there is a scarcity of convincing, direct electron microscopy data detailing the exact structure of the clusters. Finally, the magnetic properties reported, while providing evidence of metallic responses, have not yet shown any direct evidence of superparamagnetism, which is expected for the finite-sized particles. The latter would be a key signature of isolated, small particles in the titania matrix.

In the present work, we revisit this issue using aberration corrected scanning transmission electron microscopy (STEM) to directly image the ultra-small clusters in high-angle annular dark field imaging mode (HAADF) to probe the atomic structure. To explore the optimal IBS conditions, we deployed a modified procedure for the ion beam implantation compared to past work, [6] using slightly lower fluences, and a combination of beam energies to flatten the implantation profile, lowering the local cobalt percentage. The new implantation regime allows us to identify, for the first time, the strong superparamagnetic response of the small nanoclusters in air-stable samples, and directly detect the ultra-low blocking temperature (6.5 K) expected of nanomagnets approaching the quantum regime. Using X-ray circular dichroism (XMCD) and polarised neutron reflectometry (PNR) we perform element-resolved and depth-resolved studies of the magnetic properties of the cobalt nanomagnets.

2. Materials methods

2.1. Titania thin film growth on silicon

 $TiO_{2-\delta}$ films were deposited on (100)-oriented Si substrates using the atomic layer deposition (ALD) technique at 300 K. The thickness of the $TiO_{2-\delta}$ layers was 68 ± 2 nm. This thickness was selected so that the implanted layer could be well-isolated within the titania layer, away from the substrate and surface regions. Previous work on these samples has shown that the layers are amorphous for 393 K deposition, and with an off-stoichiometry parameter of $\delta\sim 0.05$ [6].

2.2. Low energy ion beam synthesis of embedded particles

The $TiO_{2-\delta}$ films were subsequently implanted with Co ions with multiple beam energies, using an ion implanter equipped with a metal vapor vacuum arc (MEVVA) ion source. The primary beam energies used were 20 keV with (3.3 \times 10¹⁵ ions/cm²) [33 kps] and 60 keV with 1 \times

10¹⁶ ions/cm² [100 kps] fluences to create a more uniform ionimplanted layer within the film. Monte Carlo calculations of the ion beam stopping depths were performed using the SRIM software [44]. Two samples were synthesised with very similar conditions. The first sample (labelled S1) was fabricated without a post-implantation heat treatment to avoid recrystallization of the films and to limit diffusion of the Co ions. Sample 2 (S2) was subjected to a gentle thermal treatment up to 450 K for 24 h. The doses in each sample were within 10% of each other. To explore other heating regimes, rapid heating studies were also conducted on S1 using an *in-situ* TEM heating stage.

2.3. Scanning transmission electron microscopy

A dual beam FIB-SEM (FEI HELIOS NanoLab G3 CX) coupled with a gas injection system (GIS) was used to prepare cross-sectional lamellae from the Co:TiO $_2$ thin films. Prior to FIB milling at 30 keV, approximately 1 μ m of carbon protective coating was deposited with electron beam surface carbon deposition to protect the TiO $_2$ surface from the gallium ions. Specimens were milled to a thickness of 100 nm or less. The lamella was welded to a Cu grid ready for TEM analysis and transferred to an aberration-corrected scanning transmission electron microscope (STEM, JEOL ARM-200F) for the phase characterization and microstructural analysis. Energy dispersive X-ray spectroscopy (EDS) attached to the STEM was used for elemental mapping of the lamella.

2.4. Measurement of magnetic hysteresis using vibrating sample magnetometry

Magnetic properties of the films were measured by a Physical Property Measurement System (PPMS) (Quantum Design, USA) using the vibrating sample magnetometry (VSM) option. The sample was mounted on a low background quartz holder with a small amount of Kapton tape positioned to give a uniform (cancelling) diamagnetic background.

2.5. NEXAFS and element resolved XMCD using X-ray spectroscopy

Near-edge X-ray absorption spectroscopy (NEXAFS) using soft X-rays was employed to measure the oxidation states of the transition metal elements. Resonant soft X-ray experiments were conducted on the ALICE instrument on the PL3 beamline at BESSY, (Berlin, Germany) for photon

energies between 300 and 800 eV [45]. X-ray magnetic circular dichroism (XMCD) measurements were performed on the same beam-line using both a total electron (TE) and total fluorescence yield detector (TFY). XMCD is the difference of X-ray absorption spectra taken with left and right circularly polarised photons.

2.6. X-ray reflectometry

X-ray reflectometry was conducted on an Panalytical X'Pert Pro reflectometer using Cu K α radiation ($\lambda=1.5406$ Å) under ambient atmosphere at room temperature.

2.7. Depth-resolved magnetometry using polarised neutron reflectometry

Spin polarised neutron reflectometry is a powerful technique to measure the magnetic depth profile of the films in absolute units, and reveal buried magnetic features. In this work, polarised neutron reflectometry (PNR) was used to determine the nanometer scale magnetization per volume in the Co:TiO2 thin films. Experiments were conducted on the NREX reflectometer at the FRMII research reactor in Munich (Germany) using monochromatic neutrons with a wavelength of $\lambda = 4.3$ Å. A polarized neutron beam (with polarization 99.99%) was incident on a sample at grazing angles $\theta=0.15\text{--}6$, and the spins-state of the reflected beam was analysed with an efficiency of 99.3%. Spin up (R₊) and spin-down (R.) reflection patterns in PNR enable a clear and direct observation of the magnetization that originates from the thin implanted layer. The reflection patterns are usually plotted as a function of the universal scattering vector, $Q_z = 4\pi sin\theta/\lambda$, where θ is the scattering angle. The Qz dependence of the reflection patterns provides information on the chemical and magnetic profile in the thin film. Quantitative fitting was performed using the SimulREFLEC software to determine the chemical and magnetic profiles [46]. The effective resolution used in the fitting was dQ/Q = 0.04. For direct qualitative analysis, it is also useful to define a quantity, the neutron spin asymmetry (SA), which is only related to the magnetic features of the thin film, as expressed in the following form:

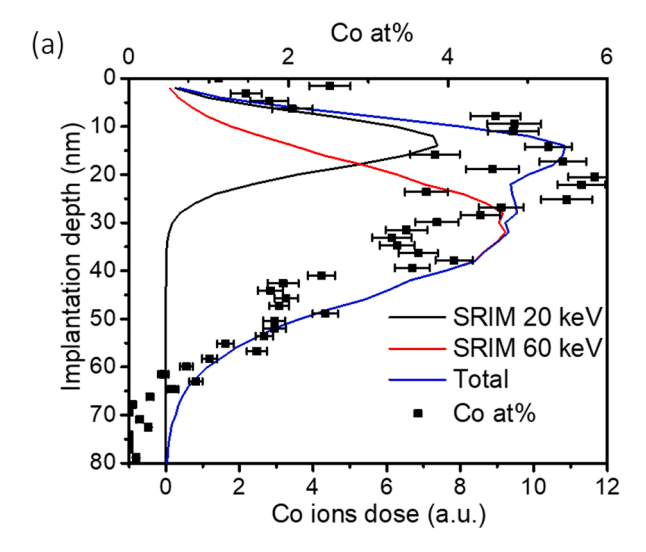
$$SA(Q) = \frac{R_{+} - R_{-}}{R_{+} + R_{-}}$$

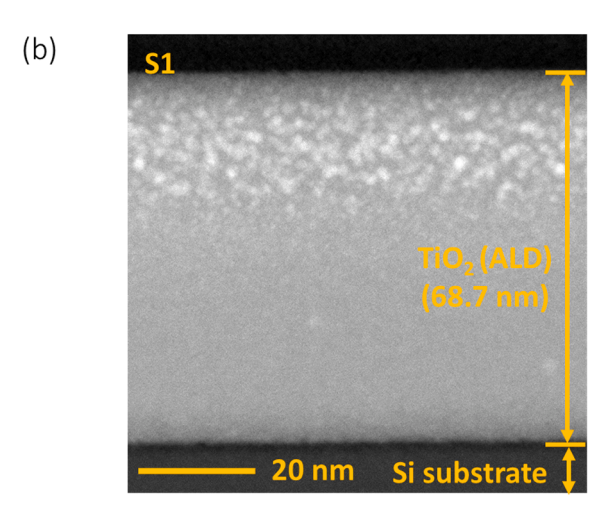
romAdditional polarized neutron reflectometry experiments were conducted using the PLATYPUS reflectometer which is a time-of-flight instrument based at the Australian Nuclear Science and Technology Organisation. These measurements are detailed in the supplementary Data-in-Brief articl.

3. Results

3.1. Implant profile and microstructure

The theoretical Monte Carlo simulations accurately model the stopping depth of the cobalt ions in the titania, in agreement with experimental data as shown by the overlapping regions in Fig. 2(a). To measure the experimental cobalt concentrations as a function of depth from the surface, EDS line profiles were collected by integrating over the region of interest in the corresponding EDS spectrum images. In both theory and in practice, the cobalt ion penetration is confined within the top 70 nm of the film and there is no spillover into the silicon substrate. The use of two ion beam kinetic energies (20 keV + 60 keV) spreads the cobalt out in a flat-topped curve centered at $\sim 30 \ \text{nm}$ below the surface. This results in a distribution of cobalt with a peak atomic percent of \sim 4-6% (assuming oxygen stoichiometry such that there is 1.950 for each Ti). Thus, the cobalt concentration is designed to be considerably lower than our previous study (16%) [6]. This results in a state where the cobalt atoms on average stop at a greater distance apart which changes the initial conditions for self-assembly to shift the system away from the





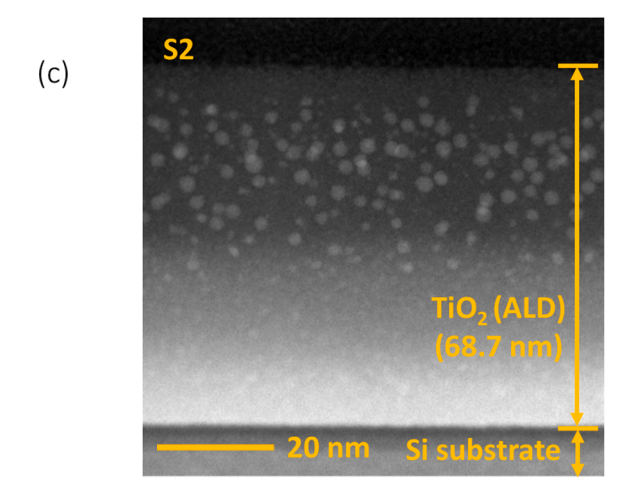


Fig. 2. (a) The penetration of cobalt ions at 20/60 keV is limited to within 100 nm of the surface as shown by the Monte Carlo SRIM simulations and experimental EDS line profile for S2. The total simulated profile is the weighted sum of the 20 and 60 keV profiles. (b) Cross-sectional HAADF images of the asimplanted sample (S1) shows non-uniformity. (c) A separate sample heat treated to 400 K shows well-defined cobalt nanoparticles embedded in the titania film.

percolation/coalescence threshold, and foster the formation of isolated nanoparticles. Further details of the EDS data are discussed below. The key point is that the lower-density cobalt distribution makes it possible to assemble isolated cobalt particles, and to detect these directly in the STEM images and study their atomic structure. Low magnification STEM cross-sections of the as-implanted (S1) and the heat treated (S2) samples are shown in Fig. 2(b) and (c). The images are both taken in high angle annular dark field (HAADF) mode where the signal intensity is approximately proportional to Z², where Z is the atomic number. The relatively higher atomic number of Co means that the embedded nanoclusters appear as bright spots and TiO2 layers appear as a medium grey background and the silicon substrate is dark. The TiO2 film is approximately 68 nm thick and the Co dopant is distributed over an approximately 35 nm deep region within the TiO2 layer. Both images show particles and non-uniform regions with very small feature sizes below 5 nm. In our experience, for other combinations of dopants and hosts, similar fluences lead to a relatively uniform lateral distribution of the implant species. The Co:TiO₂ combination is a special case because the strong inhomogeneity is an indication of the tendency for cobalt particles to self-assemble in the titania host owing to the intrinsic chemical factors which make cobalt insoluble therein. While both samples are similar, the heat treated sample (S2) shows particles that penetrate slightly deeper towards the interface with the Si substrate. This is attributed to slow diffusion and crystallization of the cobalt

To compare the chemical profiles for the other elements, Fig. 3b shows the resulting EDS elemental distribution extracted over the region of interest (indicated in Fig. 3a) for sample S1. As in the previous section, the experimental EDS line profile was extracted by averaging laterally over a 80 nm-wide region (yellow box in Fig. 3(a)) to average out the inhomogeneity in the cobalt distribution. The Ti and Si show a sharp interface. The corresponding EDS maps are shown in Fig. 3(c-f). A relatively uniform oxygen signal is observed across the titania layer, although precise quantification is not generally possible using EDS. The data for the other sample S2 exhibited the same trends. Further analysis of the line profiles was performed to calculate the integrated area under the Co and Ti profile curves. The integrated Co:Ti ratio for S1 is calculated to be 1: 12.7. This indicates that, in the sample, on average one Co atom is present per 12.7 Ti atoms. For S2, the same integration was performed and the average Co:Ti atomic ratio was found to be 1:10.3. Thus, the Co:Ti ratios in S1 and S2 are within 20% of each other, and the atomic percents of cobalt were within 10% of each other. The slightly higher ratio in the latter may indicate that some cobalt was lost during the heat treatment process, or that the initial implants were very slightly different.

Given their overall similarities, both S1 and S2 show reproducible formation of small cobalt particles in the titania matrices. Fig. 4(a) and (b) show high-resolution HAADF images for S1 and S2. Ultra-small Co nanoclusters with diameters of 0.5 to 3 nm can be observed. There is no indication of a CoO shell surrounding the particles. The particles are spherical without obvious facets. Atomic-scale imaging shows fringes appear in a few of the Co nanoclusters illustrated in the high resolution images in the Fig. 4b. Many particles do not show lattice fringes. These may be amorphous, which is often the case for ambient temperature implantation [34]. However, the presence of fringes is also dependent on the orientation of the particle and its depth within the thin foil, and so an absence of fringes does not necessarily indicate an absence of crystallinity. A small fraction of the particles are definitively crystalline in both S1 and S2. The observed lattice fringe spacing of those (inset Fig. 4 (b)) are consistent with metallic FCC cobalt as shown in the structural model of Fig. 4(b). Past work on Co implantations into SiO2 reported that a mixture of FCC and HCP cobalt metallic particles formed and that high temperature annealing tends to grow the HCP phase at the expense of FCC phase. The size distribution of the particles was extracted by analyzing the dimensions of 150 Co nanoclusters on TEM images. The resulting histograms are shown in Fig. 4(c) for S1 and S2. S1 has an average size of 1.8 \pm 0.4 nm, and S2 has an average size of 2.1 \pm 0.6 nm. This shows that the particle formation mechanism is reproducible, and the moderate heat treatment did not lead to a substantial growth in the particle size. There is also evidence of a minority of quantum-dot sized nanoclusters less than 1 nm in both S1 and S2, which may be a byproduct of the fragmentation ("inverse Ostwald ripening") process.

To test how the particles nucleated and grew in the titania host as a function of temperature, an in-situ heating experiment was performed on sample S1. Fig. 5 summarises the key results showing the average particle size. The particle sizes barely changed for temperatures below 600 K. This shows the particles are relatively stable in the titania host, and there is a high diffusion activation energy required for larger particles to grow. Fig. 6 shows the sequence of images taken during heating over the period of three hours. A moderate heat treatment of 400–450 K does not lead to substantial particle growth but does seem to subtly improve the crystallinity and definition of the nanoclusters relative to the initial implant. There is obvious visual evidence of growth above 650 K. At 750 K the amorphous titania crystallised, the surface of the film roughened, and the particles became substantially larger.

3.2. Near-edge X-ray spectroscopy and element resolved XMCD

The STEM data in the previous section clearly show that particles have formed, however it is difficult to assess whether the majority of

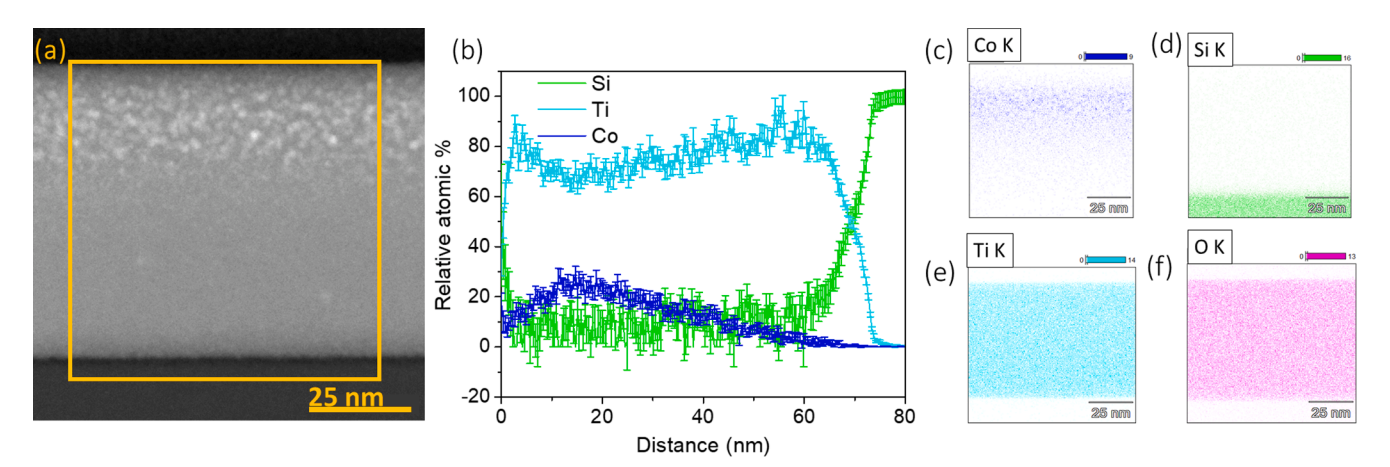
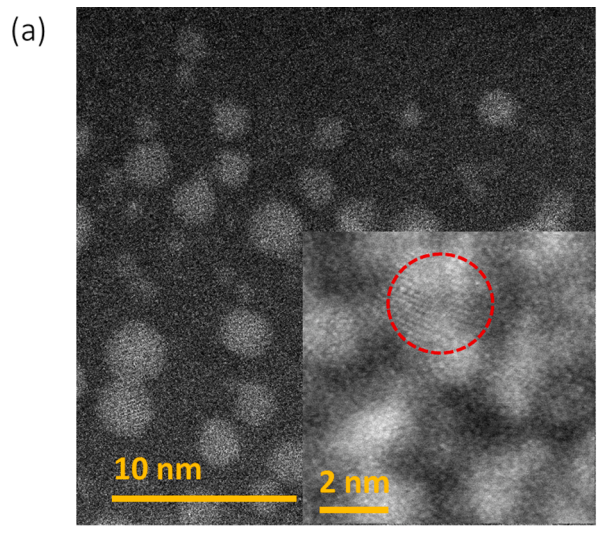
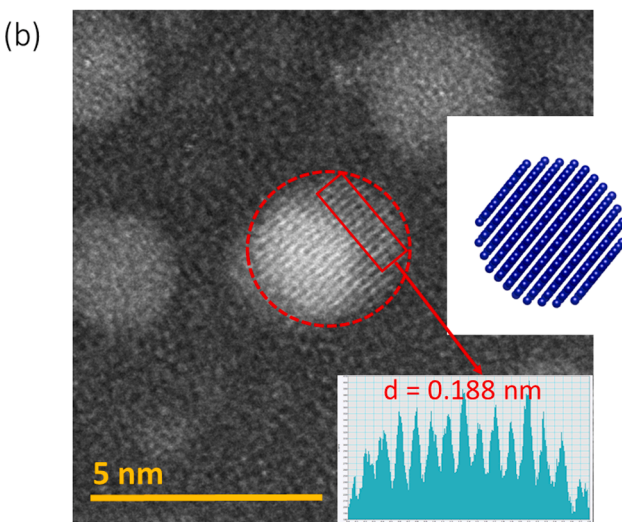


Fig. 3. (a) The cross-section TEM image showing the yellow boxed region in which rows were integrated (from top to bottom). (b) The relative amount of cobalt, silicon and titanium in the EDS line profile from (a) (left to right in (b), top to bottom in (a)). The oxygen signal is deliberately excluded in order to quantify the Ti:Co ratio more precisely. (c) The Co EDS map. (d) Si EDS map (e) Ti EDS map and (f) Oxygen EDS map. The maps are taken over the same region as shown in (a).





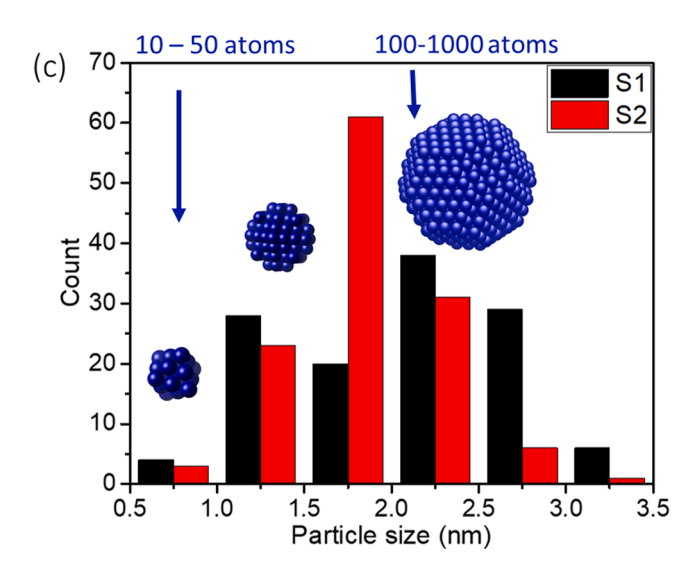


Fig. 4. (a) Higher magnification images of the particles in sample S1 and S2 (inset). (b) The high magnification images shows lattice fringes, indicating some level of crystallinity with spacing matching that of FCC cobalt. An ultra small cluster below 1 nm is also highlighted (green). (c) Histogram of the particle sizes extracted for S1 and S2 from the STEM images. The distribution is similar in both, and the average size is less than 3 nm.

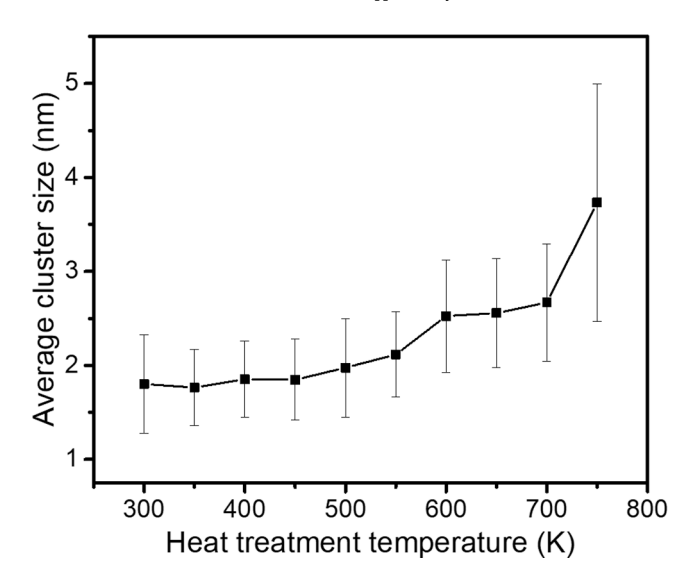


Fig. 5. The average cobalt particle size (within one standard deviation) as a function of temperature extracted during the *in-situ* heating STEM experiment.

these particles are metallic or oxides, because of the large background signal from the titania host. To investigate this question, we deployed synchrotron-based X-ray absorption spectroscopy of the L₂₃₃ edges.

Near-edge X-ray absorption fine spectroscopy (NEXAFS) is a useful technique to resolve the oxidation state of elements in a material, and is capable of probing beneath the surface unlike standard XPS. Fig. 7 shows the cobalt L-edge spectra obtained in total electron yield (TEY) and total fluorescence yield (TFY) modes. The electron yield TEY measurements are sensitive to the first few nanometers near the surface, as these depend on the escape length of electrons. In contrast, the TFY measurements probe much deeper typically to the length scale of tens of nanometers, determined by the escape length of the excited photons. For this reason, the TFY and TEY datasets for the cobalt implanted titania sample (S2) are quite different.

The surface sensitive TEY data clearly shows a multiplet that closely resembles the reference data for Co²⁺ with features at 781, 782 and 783 eV. The multiplet is strongly suppressed in the TFY data which shows a single strong broad peak, as expected from metallic Co⁰. Overall the TFY Co L-edge spectra is very similar to that of Co metal clusters in TiO2 reported in the past by Kim et al. [47]. However, there is still the hint of the ionic multiplet features. This suggests that the majority of the cobalt is metallic, however, a small surface fraction is oxidised, consistent with the TEY measurements. One of the main difference between Kim et al's work⁴⁷ and our XAS work is the type of annealing that was performed, and the level of atmospheric exposure. In Kim's study, samples were annealed in-situ in a vacuum in a crystalline titania host, and the cobalt diffused to the surface [47]. Thus the process contributed to the formation of surface metallic Co clusters that were confirmed both by XAS and XMCD. In contrast, in our study, the implantation step allowed particles to form near the surface even in the initial state, and the samples were exposed to air for the period of many months between measurements, giving them ample opportunity to oxidise. Thus, in our work, we interpret the Co²⁺ feature as the evidence of cobalt clusters that have oxidised near the surface. Our interpretation differs from some past work, where the existence of a Co²⁺ signal in the TEY NEXAFS was been taken as evidence of substitutional doping of Co onto the Ti site. In principle, the different crystal field strengths of CoO and Co_{1-x}Ti_xO₂₋ d introduce subtle changes into the Co²⁺ multiplet, however, in practice these are too similar to be discerned here. In any case, from the TFY measurements, the vast majority of the cobalt is not Co²⁺, but instead is metallic, consistent with past XPS results where argon etching was performed to reveal a large buried Co⁰ signal [6]. The magnetometry presented below also provides further evidence for the dominant role of

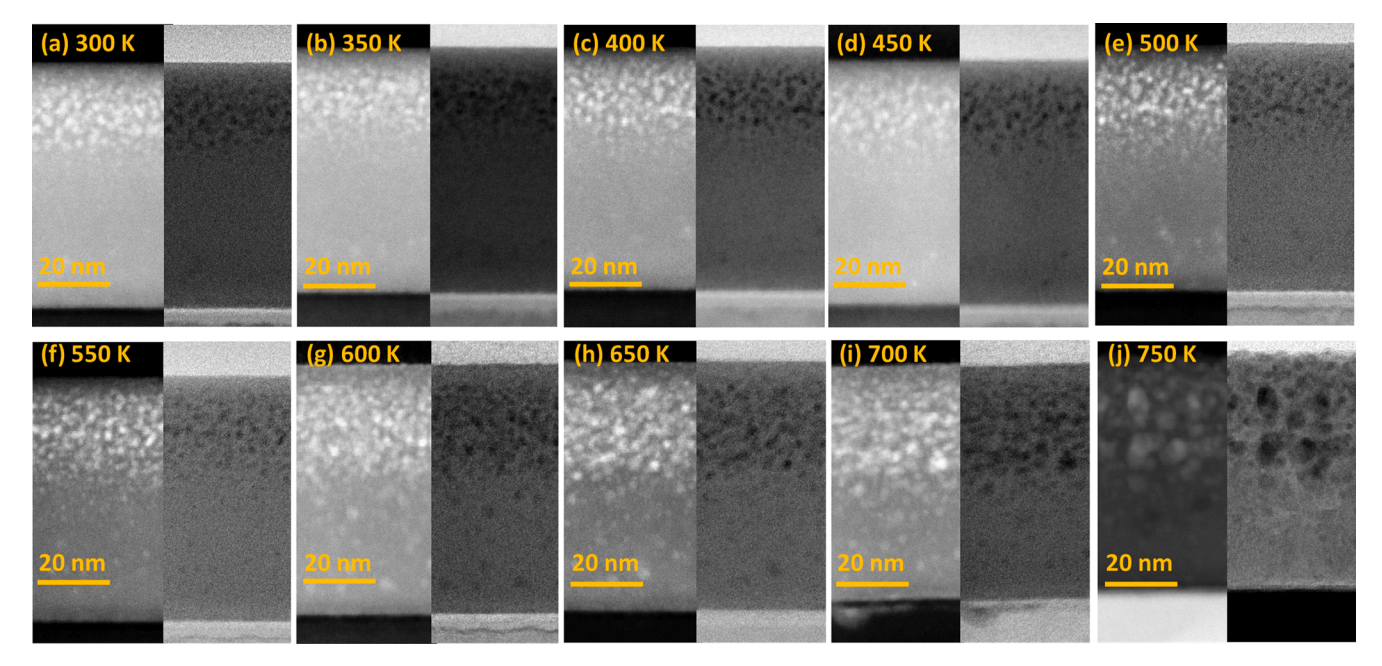


Fig. 6. STEM HAADF and bright-field image pairs taken in series during the *in-situ* heating of the ion beam implanted Co:TiO₂ sample (S1). The left hand image of each pair is the HAADF image, and the right is the bright field image which show different contrast mechanisms. The particles clearly grow in size for temperatures above 650 K. The effects below 650 K are subtle.

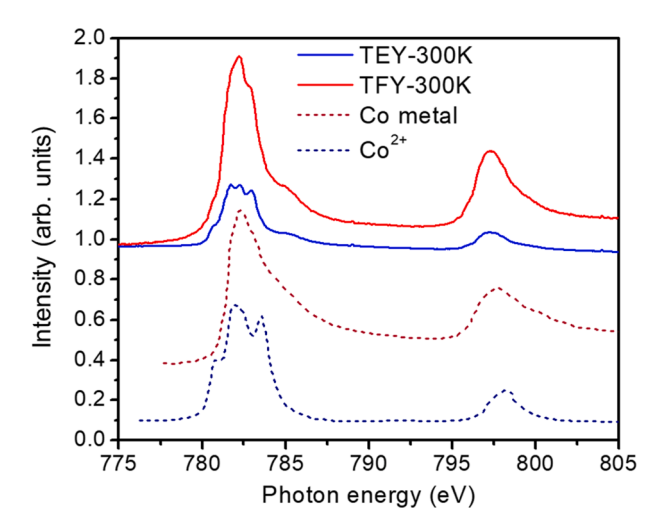


Fig. 7. NEXAFs measurements of the Co $L_{2,3}$ edge using surface-sensitive electron yield (TEY) and "bulk" sensitive fluorescence yield (TFY) measurements. The surface data shows a multiplet feature expected for ${\rm Co}^{2+}$. The bulk data is more featureless and is attributed to a larger fraction of Co metal. Reference spectra for Co metal and ${\rm Co}^{2+}$ are shown as the dashed lines beneath the experimental data for comparison and were taken from Kim et al. [Ref [45]]

small metallic cobalt particles. This set of results highlights the chemical complexity of Co:TiO_2 systems and the importance of using complementary techniques that probe beneath the surface. More direct evidence of the non-magnetic surface cobalt oxide, and the buried magnetic metallic fraction, is provided in Section E via the magnetic depth profiles extracted using polarised neutron reflectometry.

3.3. Vibrating sample magnetometry

Small metallic cobalt nanoparticles have well-known magnetic properties and are expected to exhibit superparamagnetism. In contrast, CoO particles are antiferromagnetic and are nearly "invisible" to standard magnetic probes as they possess near-zero net magnetization.

Owing to their strong magnetic response, magnetometry is therefore a very sensitive way to detect for the presence of ultra-small metallic cobalt clusters even when they are difficult to detect using STEM and other techniques.

Following the implantation of the Co ions, samples S1 and S2 were measured by VSM. In the sections below, we shall just report the magnetic properties of S1, although broadly similar properties are in Data in Brief. Typical VSM hysteresis loops at different temperatures (5 K, 10 K, 50 K, 100 K, 200 K and 300 K) are shown in Fig. 8(a). During the VSM measurement, the magnetic field was applied parallel to the sample surface. The sample shows superparamagnetic behavior, evident in the reversible S-shaped magnetization with zero coercive field. Several different field sweep rates from 2 Oe/sec to 200 Oe/sec were investigated, however, the properties were identical even at the lowest measurement temperature. The magnetization response at different temperatures can be fitted using the Langevin function describing an ensemble of superparamagnetic particles:

$$\mathbf{M} = \mathbf{M}_0 \mathbf{L}(\beta \mu \mathbf{H}) = \mathbf{M}_0 \left[\frac{1}{\tanh(\beta \mu \mathbf{H})} - \frac{1}{\beta \mu \mathbf{H}} \right]$$

where β is the inverse of the sample temperature in units of the Boltzmann constant ($\beta = 1/k_BT$), M_0 is the saturation magnetization, μ is the saturated total magnetic moment of a nanoparticle (found by summing up all the cobalt atoms in a particle of average size), and H is the external applied magnetic field. Mo is determined by the number density of the particles (n) and the average total moment per particle (μ) such that M_0 $= n\mu$. There is a good fit to the data, as shown by the solid lines in Fig. 8 (a). The parameters n and μ , however, are temperature-dependent in order to obtain a good fit, against common convention for a standard classical superparamagnet. Fig. 8(b) shows the temperature-dependence of the fitting parameters. For a simple classical superparamagnet, the temperature-dependence of the magnetization M, should be entirely determined by variation in β for temperatures above the blocking temperature. Instead, for the ultra-small cobalt particles in titania, the magnetization increases more strongly than expected, and the shape of the loop also varies more than expected with temperature, indicating that both M_0 and μ are variables. This can be rationalised if there is a hidden fraction of magnetic particles with a magnetic moment that only

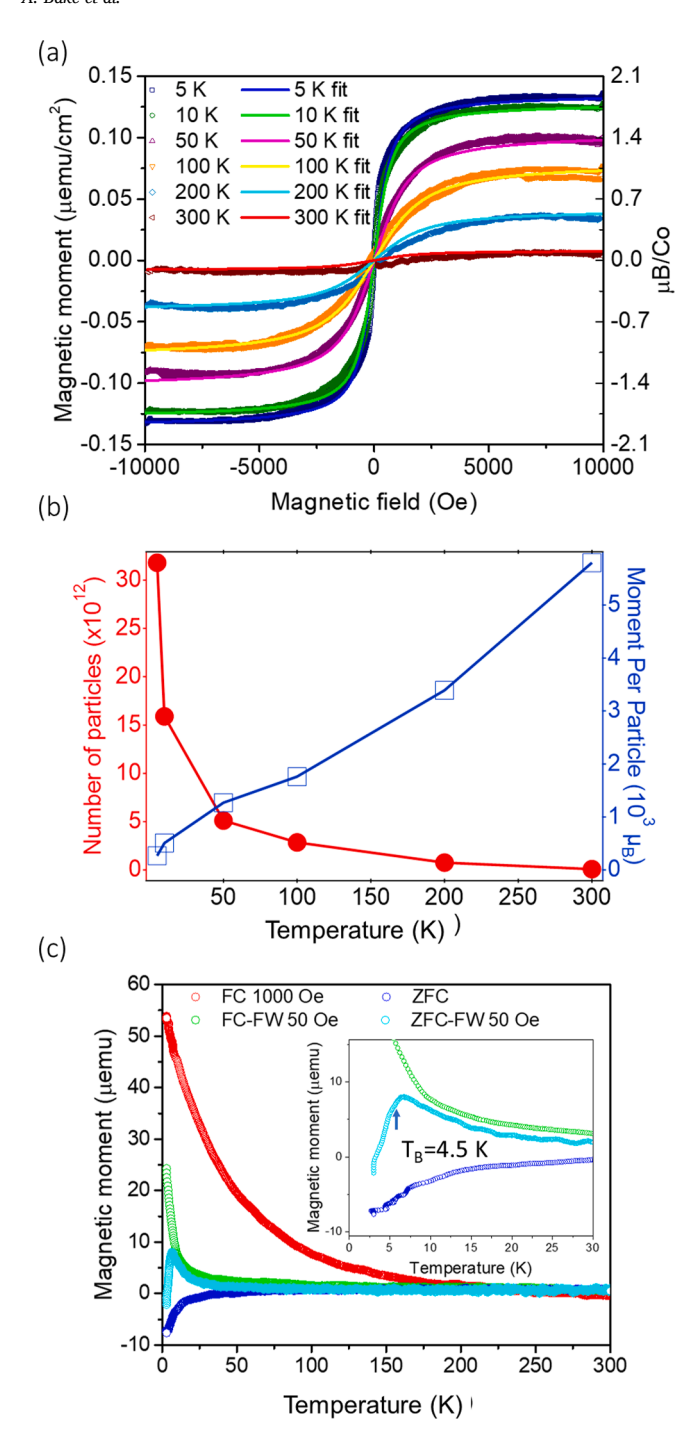


Fig. 8. (a) Superparamagnetism is observed in the magnetic hysteresis loop for sample S1 at various temperatures. The solid lines are the fits to the data using the Langevin expression in the text. (b) The fitting parameters used in latter figure show a strong temperature dependence which would not be expected for a simple classical superparamagnet. (c) Temperature dependence of the magnetization under different field-cooling regimes. The inset show the blocking temperature of 4.5 K.

appears strongly at low temperature so that the effective number of particles (n) increases at low temperature. This could arise if some particles are not ferromagnetically ordered at high temperature, but only become magnetically ordered at low temperatures. This may occur because the exchange interactions in the particles are weaker than that of normal cobalt. Such behavior can be expected of very small cobalt particles where the electronic structure is affected by quantum confinement effects. For example, sufficiently small cobalt particles are

predicted to exhibit a band-gap, and to become insulating⁸. The nature of the exchange interactions in the insulating state will be considerably different. Another effect is the well-known universal finite-size scaling of the Curie temperature which could lead to similar observables. In either case, consistent with this idea of weaker magnetic exchange in the smaller particles, the average effective magnetic moment per particle (superspin) decreases slightly with decreasing temperature, even though the net moment $(M_0 = n\mu)$ increases. Assuming that each cobalt contributes $\sim 2~\mu_B$ per atom, this implies that very small clusters (average size $\sim 100-200$ atoms) become more dominant at low temperature, whereas at high temperature the magnetism is contributed only by a small fraction of much larger particles with > 1000 atoms. As the sample has a distribution of particle sizes, the fitting parameters are affected by the laws of averaging, and so one should regard M_0 and μ as weighted ensemble averages, rather than reflecting the absolute values for any single particle. Nevertheless, the variations in these parameters hint at some interesting physical phenomena, either interactions between the particles in the matrix, or quantum effects, which would explain the variation in the magnetization [1]. It is also possible that an intrinsic DMOS Co_{1-x}Ti_xO_{2-d} plays a role, or that magnetic Ti³⁺ is formed, however the PNR data shown in Section E does not favor this perspective, as shall be discussed later.

To investigate the temperature dependency and determine the blocking temperature, additional field cooled (FC) and zero-field cooled (ZFC) measurements were performed. Fig. 8(c) shows the different curves for different field cooling regimes. At large fields, the response of the system resembles that of a paramagnet with a magnetization that scales roughly as 1/T^N. For a simple paramagnet, the scaling parameter should be N=1, however here $N\sim 0.15$ indicates that this magnetic system differs strongly from the simple paramagnetic Curie-Weiss law. Furthermore, the measurements at smaller fields reveal a cusp in the ZFC data, as shown in the inset. This cusp is expected near the blocking temperature of the superparamagnetic ensemble. In many past experimental studies, the blocking temperature is taken at the peak of the ZFC data, but according to a rigorous theoretical treatment, the $T_{\rm B}$ should be shifted slightly down from the peak in a polydisperse sample [48]. Using the fitting method from Ref. [48], the blocking temperature is 4.5 K (Data in Brief), which is significantly smaller than previously reported values for cobalt nanocrystals formed in titania [49]. This is consistent with the smaller particle size possible using the IBS method. Using a coarse-approximation one can estimate the particle volume using the relation:

$$K_A V = 25 k_B T_B$$

where V is the volume, K_A is the anisotropy, k_B is the Boltzmann constant and $T_{\rm B}$ is the blocking temperature. For standard metallic cobalt $K_{\rm A} \sim$ 4.5×10^6 erg/cm³. This relationship was shown to be valid for particles as small as 8–10 nm, [49] however it does not appear to have been tested for even smaller particles. Applying this value to the current particles, the volume should be 5 nm³, and assuming a spherical particle, the diameter should be 2.1 nm. The fact that this is in good agreement with the STEM data suggests that the anisotropy parameter of the cobalt nanoparticles is very similar to the nominal value in the bulk metal. More detailed fitting was performed using the method described in Ref. [48] and is shown in the Data in Brief, leading to a similar determination of the blocking temperature and anisotropy constants. This in turn suggests that, at these particle sizes, the orbital magnetic moment is still mostly quenched because if L were $\gg 0$, one would expect a sizable additional anisotropy. These findings are in broad agreement with past results for ultra-small cobalt clusters which showed that L only became sizable once the cluster size became smaller than 10 atoms [2]. On the other hand, the size of the cobalt particles in this work means that they approach the quantum confinement regime where the electronic structure of cobalt is no longer metallic. If band electrons are key to mediating magnetic exchange, the strong confinement effect in the small

particles may yield a strong variation in the exchange constants, and therefore in the temperature dependency of the net magnetization. The strong temperature dependency of the magnetization was not observed in larger (8 nm) cobalt particles in titania [49], suggesting that it is a unique property of the ultra—small cobalt nanomagnets formed using the IBS method. Traditional magnetometry is sensitive to the net magnetic moment from all sources, and background and unwanted impurities can therefore contribute. To confirm that the magnetic properties originate directly from the cobalt nanomagnets, we complemented the VSM measurements with more advanced magnetic techniques including XMCD and PNR. Unlike the VSM measurements described earlier, which probe the entire sample volume and extract the average properties, both of these more advanced techniques can yield information uniquely for the cobalt region.

3.4. D. Element-resolved X-ray circular dichroism

To detect the elemental magnetic moment on the cobalt atom, we performed XMCD measurements on S2 in both electron yield (TEY) and fluorescence yield (TFY) modes. Fig. 9 shows the TFY XMCD signal that appears on the cobalt $L_{2,3}$ resonance and varies with temperature. This confirms that the cobalt in the TiO₂ is magnetic, as expected. Moreover, our XMCD spectra are similar to the clear Co L-edge XMCD reported by Mamiya et al., [50] as well as identified in the previous literature⁴⁷. There is only the merest hint of the oxide multiplet structure with features at 781, 782 and 783 superimposed on a strong primary single peak. The latter suggests the XMCD primarily arises from metallic cobalt. From the ratio of the L_2 / L_3 peaks it is sometimes possible to quantify

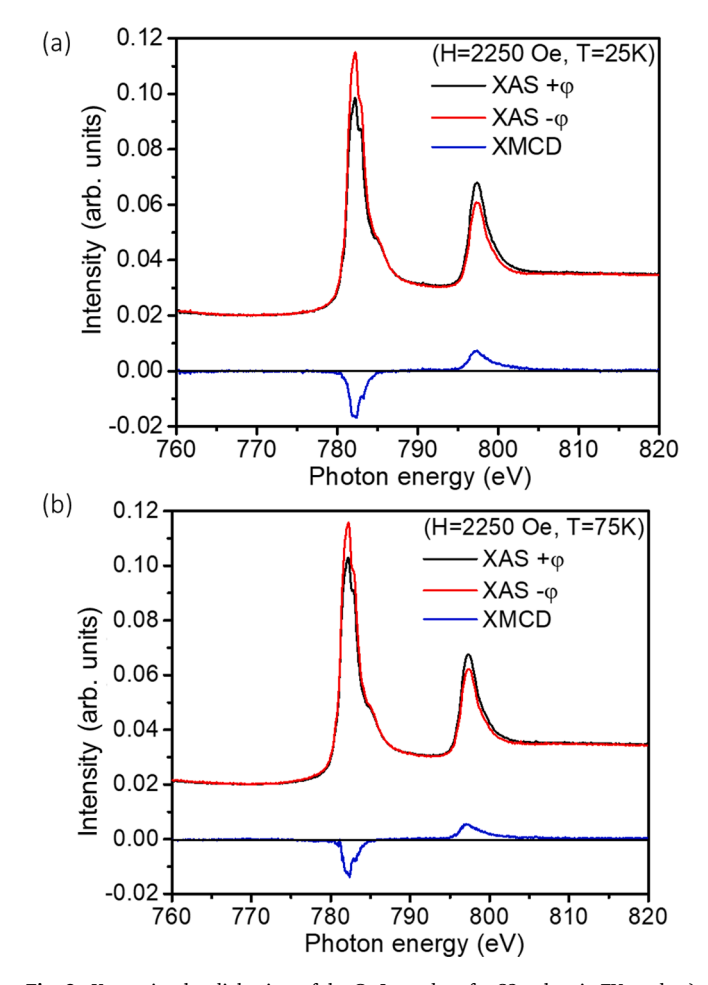


Fig. 9. X-ray circular dichroism of the Co $\rm L_{2,3}$ edges for S2, taken in FY mode a) 25 K and b) 75 K.

the absolute moment, spin moment and angular moment. For this purpose, electron yield measurements are essential. Unfortunately, the XMCD signal was not detectable in the TEY measurements. This was attributed to the presence of oxidised cobalt which produced a non-magnetic "dead" layer, but only within the first few nanometres of surface of the film, because the signal detected in TFY is dominated by non-oxidised cobalt. It is well known that quantification of TFY data is complicated by self-absorption leading to errors as large as 50% in the values [51]. Nevertheless, we still provide an estimate using the sum rules to estimate L and S [52]:

$$\langle L_Z
angle = -2n_h \cdot rac{\int\limits_{L_3+L_2} [I^{\uparrow \uparrow} - I^{\uparrow \downarrow}] d\omega}{\int\limits_{L_3+L_2} [I^{\uparrow \uparrow} + I^0 + I^{\uparrow \downarrow}] d\omega}$$

$$\langle S_Z \rangle = -\frac{3}{2} n_h \cdot \frac{\int\limits_{L_3} [I^{\uparrow \uparrow} - I^{\uparrow \downarrow}] d\omega - 2 \int\limits_{L_2} [I^{\uparrow \uparrow} - I^{\uparrow \downarrow}] d\omega}{\int\limits_{L_3 + L_2} [I^{\uparrow \uparrow} + I^0 + I^{\uparrow \downarrow}] d\omega}$$

where $I^{\uparrow\uparrow}$ and $I^{\uparrow\downarrow}$ are the L-edge excitation spectrum measured with the photon angular which is circularly polarised to give momentum parallel $(I^{\uparrow\uparrow})$ or anti-parallel $I^{\uparrow\downarrow}$ to sample magnetization; I_0 linear polarized signal taken as the average of $I^{\uparrow\uparrow}$ and $I^{\uparrow\downarrow}$; ω is the phonon energy and n_h is the number of 3d vanancies ($n_h = 3$ for 3d7). The formula above assumes that, owing to the particulate nature and powder-like nature of the cobalt, the spin-quadrupole coupling averages to zero. The estimate from the 25 K data is that S = 0.73 and L = 0.02, giving a net moment of 1.47 μB per cobalt atom which is about 20% lower than that estimated from the magnetometry. This near zero orbital moment suggests that quenching of the angular momentum has occurred in the clusters, as expected based on the particle size distribution where the major of clusters contain 100 – 1000 atoms, lying in a size range where the orbital moment is quenched. We point out that both the magnetometry and XMCD are the volume-average over the whole cobalt ensemble, and therefore non-magnetic cobalt will also be detected and lower the average. As oxide regions, and lightly doped regions appear not to contribute to the magnetic moment, the latter will lower the average. Therefore, to quantify the peak magnetic moment of cobalt below the titania surface only in the superparamagnetic regions, and to test the latter hypothesis, PNR was conducted.

3.5. E. Magnetic depth profile with polarised neutron reflectometry

PNR is a powerful small-angle neutron scattering technique for detecting the magnetic and chemical depth-profiles in thin films, interfaces and surfaces [53]. This specialised technique offers a real-space resolution on the scale of nanometres, and is capable of penetrating below the surface of a material to measure the magnetization in absolute units (μ_B per cm³). Simultaneously, the technique is also sensitive to the chemical depth-profile of a sample, as this has an impact on the nuclear scattering length density that partially determines the neutrons refractive index. The combination of nuclear and magnetic sensitivity makes PNR a useful technique to quantify the magnetic properties of the buried cobalt implant layer, while simultaneously testing for the presence of any non-magnetic "dead" layers.

Fig. 10(a) and (b) show polarised neutron reflectometry patterns for the cobalt-implanted $TiO_{2-\delta}$ thin film (S2) at 5 K and 300 K, respectively under an applied field of 4.5 kOe. The sharp Kiessig fringes observed in the PNR data indicate that the interfaces within the sample are of high-quality, and hence, very smooth. In turn, this implies that the implanted particles are so small that they manifest effectively as a homogenous doping layer when viewed through the lens of the specular PNR technique, which laterally averages over the entire layer. Complementary specular X-ray reflectometry is shown in the Data in Brief. The contrast for the layers in the neutron reflectometry experiment is far greater than

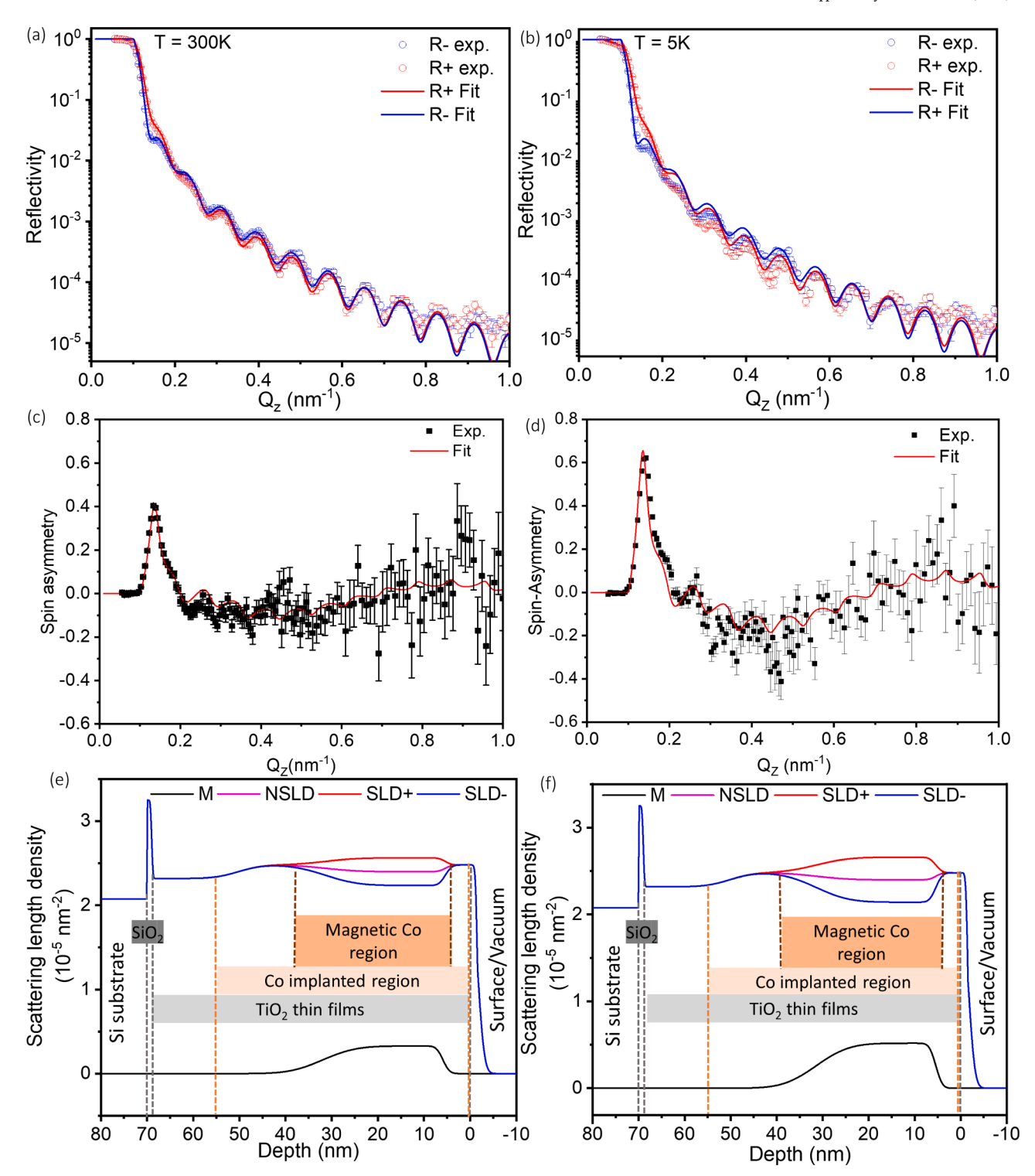


Fig. 10. a) Clear Kiessig fringes and spin asymmetry are observed in the polarised neutron reflectometry pattern for sample S2 at 300 K in a field of 4.5 kOe. The points are the data. The solid lines are fits to the data. b) The PNR pattern at 5 K shows an increased spin asymmetry for sample S2 in 4.5 kOe. c) The neutron spin asymmetry, and best-fit to the 300 K data. d) Neutron spin asymmetry at 5 K and best fit. e) The best fit SLD model to the neutron data at 300 K. f) The best-fit SLD Model to the PNR data at 5 K.

in the X-ray reflectometry in this case, because neutrons offer sensitivity to low atomic number elements (e.g., oxygen) and also magnetism. Indeed, there is clear evidence of magnetic contribution to the neutron reflectometry patterns, as shown by the difference in the spin up (R_+) and spin down (R_-) reflectivity patterns. Experimentally, the strong neutron spin asymmetry shown in the raw data of Fig. 10(c) and (d) confirms a large magnetization in the near-surface region (top 40 nm) of

the sample across a temperature range from 5 K to 300 K. As temperature decreases, the spin asymmetry increases accordingly, in line with the increased magnetic moment detected using VSM in the previous section. The Q_z -dependency of the spin asymmetry encodes the spatial dependency of the magnetic distribution. The SA shows at peak a low Q and oscillations at higher Q which can be described by the model of the magnetic implant layer discussed later. The maximum in the SA occurs

at approximately $Q_z = 0.12 \text{ nm}^{-1}$. It exceeds 40% at 300 K and increases up to 65% at 5 K, comparable to the values in past work [6]. To fit the PNR patterns quantitively, we use similar methods as implemented in past work [4,6,32,54-55]. In particular, to model the complex implantation profile, we use a multi-slice model of the titania thin film divided into the components shown in Fig. 10(e) and (f), and used linear leastsquares fitting to obtain best fits to the data. The magnetic moment, depth of the implant layer and nuclear SLD of the implant layer were used as free parameters. The overall thickness of the layer, and the nuclear SLD of the titania film were constrained to the values consistent with the TEM imaging (within \pm 3 nm), and the relative atomic percentages of cobalt and titanium were confined to the values determined from EDS mapping (within \pm 5%). The Q_z dependency and the intensity of the reflectometry patterns are well-described by the best-fit models which result in the solid lines in Fig. 10(a) and (b) which match the experimental data points well. Furthermore, both the experimental data and best-fit models show intensity oscillations as a function of Qz associated with the finite thickness of the film, which causes neutron interference. The SLD profiles corresponding to each dataset are presented in Fig. 10(e) and (f), showing the nuclear and magnetic contributions. The fitted nuclear SLD of the TiO₂ layer is $2.4 \times 10^{-6} \, \text{Å}^{-2}$ which is within 5% of perfectly stoichiometric TiO2, indicating the film has high density and only slight off-stoichiometry. There is a small variation, within a few percent, of the nuclear SLD of the TiO2 layer over the implanted region. The variation is smaller than in past work, and is attributed to a gentler, broader ion beam implant profile which produces less local cobalt concentration, and also less vacancies and knock-on events. From the plots of the fitted SLD profiles, it is clear that a large magnetization is present in a ~ 35 nm implanted layer, evident in the bifurcation between the SLD + and SLD- profiles, and this accounts for the Q-dependence of the spin asymmetry. The position, thickness and uniformity of this magnetic layer, corresponds to the expectation from the implantation conditions.

While the majority of the implanted particles are magnetic in the 35 nm implant layer, the lightly doped regions far below the surface (>50 nm) do not contribute a detectable magnetic signature to the PNR SLD profile. The EDS data shows some cobalt at the latter depths, but it is far reduced compared to the main implant layer. The lack of magnetization in the deeper regions implies that a threshold cobalt atomic concentration (i.e. the solubility limit) is needed before cobalt nanoparticles self-assemble, and that self-assembly of metallic particles is a key ingredient in regions with high magnetization. In the lightly doped regions, no obvious particles were observed in TEM, and this is consistent with the presence of isolated cobalt single atom dopants formed below the solubility limit. To confirm this point, additional PNR experiments were conducted on lightly- implanted TiO2 films using the PLATYPUS reflectometer (see supplementary Data-In-Brief article). These demonstrate that a net magnetization is detectable in samples with 5 atom % of cobalt, however samples with 2-3 atom % do not have a detectable magnetization. This confirms that a threshold amount of cobalt is required for magnetism, and that the intrinsic DMOS response from isolated dopants in the sample is weak, whereas the assembly of metallic particles is advantageous for forming a high magnetization. Returning to the multi-implanted samples in Fig. 10, it is clear that the topmost region within 5-8 nm of the surface of the film is non-magnetic, consistent with the XMCD measurements. Similar surface "magnetic dead layers" have been reported previously for cobalt-doped TiO2 [56]. In the current case, we attribute this magnetically dead layer to the oxidation of nearsurface Co particles caused by ambient exposure, leading to the formation of non-magnetic CoO, which are not fully protected by the passivating properties of the titania host material. However, this oxidation only affects a tiny minority of the particles, those within a few nanometers of the surface, whereas the majority of the particles deeper than 8 nm are well-protected from oxidation. Indeed, the largest magnetization appears from 8 to 40 nm deep into the sample, exactly where the metallic clusters are observed in the TEM imaging. These magnetic

regions, which contain over 80% of the cobalt, also dominate the distinctive magnetic signal observed in Sections C and D.

In addition to probing the depth-distribution of the magnetic layers, PNR can be used to provide a more accurate measurement of the magnetic moment per cobalt atom since it can resolve variation within specific depths within the sample. Using the cobalt atomic percentages detected by TEM, the PNR magnetization can then be converted into a moment per cobalt atom. As shown in Fig. 10(e) and (f), the magnetization is fairly uniform from 10 nm to 30 nm beneath the surface of the film, consistent with the relatively uniform cobalt distribution designed using the precise IBS conditions. The peak moment per each Ti_{1-x}:Co_x unit is 0.58 μ_B at 5 K and 4.5 kOe. Based on the atomic percentages extracted from TEM , this corresponds to 2.6 \pm 0.8 μ_B per cobalt atom, in broad agreement with the past report [6]. The cobalt clusters therefore appear to have a larger moment than bulk cobalt (commonly reported at $1.7 \mu_B$). The enhanced moment is attributed to the ultra-small particle size, and is broadly consistent with past DFT calculations⁸ and measurements of very small cobalt clusters [1].

4. Discussion

The present work opens up a way to safely protect, and therefore functionalise ultra-small transition metal particles. The mechanism for their stability in titania warrants some further discussion.

Although previous NEXAF and XAS studies have detected metallic features in TiO₂ [6,41,47,57], until now there has been little direct proof of ultra-small clusters forming. Furthermore, there been little explanation as to why the cobalt phase self-assembles in the titania host, and why cobalt rather than cobalt oxide is formed. An examination of the thermodynamics offers a potential explanation. It is remarkable that the cobalt clusters embedded in the titania remain metallic, given the reactivity of cobalt surfaces, which yields a spontaneous reaction (with a negative Gibbs energy $\Delta G < 0)$

$$\text{Co} + \frac{1}{2}\text{O}_2 \rightarrow \text{CoO}, \, \Delta G = -215 \text{ kJ } @300 \text{ K}$$

The key seems to be that the Co is implanted into sub-stoichiometric titania. There are a range of sub-stoichiometric Ti oxides for which thermodynamic data are available. These include $\rm Ti_2O_3$ and $\rm Ti_8O_{15}$. In all cases the sub-stoichiometric oxides are sufficiently reducing so that (in the absence of free $\rm O_2$) the reactions below would be favored at 300 K. For example:

$$CoO + Ti_8O_{15} \rightarrow Co + 8TiO_2$$
, $\Delta G = -130 \text{ kJ } @300 \text{ K}$

and

$$CoO + Ti_2O_3 \rightarrow Co + 2TiO_2$$
, $\Delta G = -129 \text{ kJ } @ 300 \text{ K}$

Therefore, provided the titania matrix remains impermeable to air, the Co nanoclusters sufficiently far below the surface will be held in a reduced metallic form. In fact, the chemical reactions will tend to prefer to convert off-stoichiometric ${\rm TiO}_{2\cdot\delta}$ to ${\rm TiO}_2$, at the expense of forming CoO. There is strong evidence that a few nanometers of ${\rm TiO}_{2\cdot\delta}$ is sufficient to block ambient oxygen, and thus beneath the surface, the cobalt clusters are stable.

The ultra-small clusters also exhibit some features which suggest they are small enough to approach the regime where quantum effects may become important. The first effect is that superparamagnetic behavior of the cobalt ensemble shows effects that cannot be fully described by the classical Langevin equation. In particular, it appears that a large number of very small particles become increasingly magnetic at low temperature, at a rate greater than the classical expectation values. The second piece of evidence is the observation that the cobalt nanoclusters have an enhanced magnetic moment (>2 μ_B) compared to bulk cobalt metal (1.7 μ_B). Previously this was attributed to the role of TiO $_{2-x}$ oxygen vacancy defects and possible d_0 magnetism in the sample [6]. However, given the overall similarity with other ultra-small cobalt

clusters in vacuum, it seems more likely that it is an intrinsic effect from the ultra-small clusters approaching the quantum regime.

5. Conclusions

Our study has shown the possibility of fabricating ultra-small nanoclusters with sizes below 3 nm near the $\text{TiO}_{2-\delta}$ surface using IBS. Compared to existing methods, the particles produced by this method are much smaller. The advantage of IBS is that ion beams allow for focused patterns and lithography, which can be advantageous in electronics and data storage applications.

Normally, metallic particles (aside from noble metals) cannot be stable in air for long periods of time because they oxidise in ambient conditions, but it appears that the IBS method can produce particles that survive in the metallic form.

Theoretically, the orbital angular momentum of an ultra-small magnetic cobalt cluster should remain unquenched. This may be one of the contributions leading to the enhanced magnetic moment observed in this work. However, there could be several advantages in attempting to fabricate even smaller cobalt clusters using modified ion implantation steps to optimise the "inverse Ostwald ripening" phenomenon. Future work should aim to confirm this and harness the intrinsic anisotropy of cobalt nanoarchitectures which may enable a new generation of nanomagnetic functionality.

Author contribution

Abdulhakim Bake: Methodology, Data curation, Investigation, Data analysis, Writing original draft. David Cortie: Cconceptualisation, Methodology, Data curation, Supervision, Project administraton, Writing - reviewing and editing. Peter Evans, Zeljko Pastuovic: Methodology, Investigation, Writing - reviewing and editing, Supervision, Validation. Michael Cortie: Investigation, Formal analysis. Sara Callori, MD Rezoan Rahman and Grace Causer: Data curation, Formal analysis, Methodology, Radu Abrudan, Florin Radu, and Yury Khaydukov: Methodology, Validation, Data analysis. Mitchell Nancarrow: Methodology, Reviewing and editing. Karen Livisey: Methodology, Investigation. David Mitchell: Methodology. Xiaolin Wang: Resources, Project administration, Writing - review and editing.

Declaration of Competing Interest

The authors declare that they have no known competing financial interests or personal relationships that could have appeared to influence the work reported in this paper.

Acknowledgements

DC acknowledges the support of the Australian Research Council (ARC) via DE180100314 and UOW-ANSTO seed grant. This work was partly supported by the ARC Centre for Excellence in Future Low Energy Electronics (CE170100039). This research used the JEOL JEM-ARM200F funded by the ARC LIEF grant (LE120100104). Ion beam implantation was performed using the facilities at the Centre for Accelerator Science (CAS), at the Australian Nuclear Science and Technology Organisation (P7437). Research activities at the CAS including operation of the LEII/accelerator systems are funded by the NCRIS program by the Australian Government. Part of this research was undertaken on the Soft X-ray spectroscopy beamline at the BESSY, Helmholtz Zentrum, Berlin. Travel support was provided by the Australian Synchrotron's International Access Funding Program. This work is partially based on experiments performed at the NREX instrument operated by Max-Planck Society at the Heinz Maier-Leibnitz Zentrum (MLZ), Garching, Germany. YK would like to acknowledge financial support of German Research Foundation (Deutsche Forschungsgemeinschaft, DFG, Project No. 107745057 - TRR80). AB acknowledges the support of an post-graduate research award from the Australian Institute of Nuclear Science and Engineering (AINSE).

Appendix

see Table 1

References

- [1] I.M.L. Billas, A. Châtelain, W.A. de Heer, Science 265 (1994) 1682.
- [2] P. Gambardella, S. Rusponi, M. Veronese, S.S. Dhesi, C. Grazioli, A. Dallmeyer, I. Cabria, R. Zeller, P.H. Dederichs, K. Kern, C. Carbone, H. Brune, Science 300 (2003) 1130–1133.
- [3] R. Miranda, F. Ynduráin, D. Chandesris, J. Lecante, Y. Petroff, Phys. Rev. B 25 (1982) 527–530.
- [4] D.L. Cortie, G.L. Causer, K.C. Rule, H. Fritzsche, W. Kreuzpaintner, F. Klose, Adv. Func. Mat. 30 (2020) 1901414.
- [5] I.G. Rau, S. Baumann, S. Rusponi, F. Donati, S. Stepanow, L. Gragnaniello, J. Dreiser, C. Piamonteze, F. Nolting, S. Gangopadhyay, O.R. Albertini, R. M. Macfarlane, C.P. Lutz, B.A. Jones, P. Gambardella, A.J. Heinrich, H. Brune, Science 344 (2014) 988.
- [6] D.L. Cortie, Y. Khaydukov, T. Keller, D.J. Sprouster, J.S. Hughes, J.P. Sullivan, X. L. Wang, A.P. Le Brun, J. Bertinshaw, S.J. Callori, R. Aughterson, M. James, P. J. Evans, G. Triani, F. Klose, ACS. Mat. Int. 9 (2017) 8783–8795.
- [7] X. Ding, X. Cui, C. Xiao, X. Luo, N. Bao, A. Rusydi, X. Yu, Z. Lu, Y. Du, X. Guan, L.-T. Tseng, W.T. Lee, S. Ahmed, R. Zheng, T. Liu, T. Wu, J. Ding, K. Suzuki, V. Lauter, A. Vinu, S.P. Ringer, J.B. Yi, ACS. Mat. Int. 11 (2019) 43781–43788.
- [8] B. Farkaš, N.H. de Leeuw, Nanotechnology 31 (2020), 195711.
- [9] J. Ahmed, S. Sharma, K.V. Ramanujachary, S.E. Lofland, A.K. Ganguli, J. Coll. Int. Sci. 336 (2009) 814–819.
- [10] K. Ahmed, I. Tariq and S. U. J. P. A. B. Siddiqui, 2016, 5.
- [11] S.M. Ansari, R.D. Bhor, K.R. Pai, D. Sen, S. Mazumder, K. Ghosh, Y.D. Kolekar, C. V. Ramana, Appl. Surf. Sci 414 (2017) 171–187.
- [12] A. Attri, A. Kumar, S. Verma, S. Ojha, K. Asokan, L. Nair, Nano. Res. Let. 8 (2013)
- [13] B.-X. Chung, C.-P. Liu, Mat. Let. 58 (2004) 1437-1440.
- [14] L.G. Jacobsohn, M.E. Hawley, D.W. Cooke, M.F. Hundley, J.D. Thompson, R. K. Schulze, M. Nastasi, J. Appl. Phys. 96 (2004) 4444–4450.
- [15] S.A. Kahani, H. Molaei, J. Coordi. Chem. 66 (2013) 4430-4440.
- [16] S.S. Kalyan Kamal, P.K. Sahoo, M. Premkumar, N.V. Rama Rao, T. Jagadeesh Kumar, B. Sreedhar, A.K. Singh, S. Ram, K. Chandra Sekhar, J. All. Comp. 474 (2009) 214–218.
- [17] A. Kotoulas, C. Dendrinou-Samara, C. Sarafidis, T. Kehagias, J. Arvanitidis, G. Vourlias, M. Angelakeris, O. Kalogirou, J. Nano. Res. 19 (2017) 399.
- [18] N. Mir, A. Heidari, M. Salavati-Niasari, N. Pourmolai, J. Mat. Sci. Mat. Elec. 27 (2016) 10747–10753.
- [19] C. Osorio-Cantillo, A.N. Santiago-Miranda, O. Perales-Perez, Y. Xin, J. Appl. Phys. 111 (2012) 07B324.
- [20] I.W. Park, M. Yoon, Y.M. Kim, Y. Kim, J.H. Kim, S. Kim, V. Volkov, J. Mag. Mag. Mat. 272–276 (2004) 1413–1414.
- [21] N. Sahiner, H. Ozay, O. Ozay, N. Aktas, Appl. Cat. B. Env. 101 (2010) 137-143.
- [22] M. Salavati-Niasari, F. Davar, M. Mazaheri, M. Shaterian, J. Mag. Mag. Mat. 320 (2008) 575–578.
 [23] M. Salavati-Niasari, Z. Fereshteh, F. Davar, Polyhedron 28 (2009) 1065–1068.
- [24] T. Senthamarai, V.G. Chandrashekhar, M.B. Gawande, N.V. Kalevaru, R. Zboril, P. C.J. Kamer, R.V. Jagadeesh, M. Beller, Chem. Sci. 11 (2020) 2973–2981.
- [25] G. Seong, S. Takami, T. Arita, K. Minami, D. Hojo, A.R. Yavari, T. Adschiri, J. Supercrit. Fluid 60 (2011) 113–120.
- [26] N.C. Shin, Y.-H. Lee, Y.H. Shin, J. Kim, Y.-W. Lee, Mater. Chem. Phys. 124 (2010) 140–144.
- [27] H. Shirai, T. Kinoshita, M. Adachi, Aerosol Sc. Tech. 45 (2011) 1240–1244.
- [28] Y. Song, H. Modrow, L.L. Henry, C.K. Saw, E.E. Doomes, V. Palshin, J. Hormes, C.S. S.R. Kumar, Chem. Mat. 18 (2006) 2817–2827.
- [29] C. Wang, X. Han, X. Zhang, S. Hu, T. Zhang, J. Wang, Y. Du, X. Wang, P. Xu, J. Phys. Chem. C 114 (2010) 14826–14830.
- [30] V.V. Yanilkin, G.R. Nasretdinova, Y.N. Osin, V.V. Salnikov, Electrochem. Act. 168 (2015) 82–88.
- [31] W.H. Meiklejohn, C.P. Bean, Phys. Rev. 105 (1957) 904–913.
- [32] D.L. Cortie, Y.W. Ting, P.S. Chen, X. Tan, K.W. Lin, F. Klose, J. Appl. Phys. 115 (2014), 073901.
- [33] V. Skumryev, S. Stoyanov, Y. Zhang, G. Hadjipanayis, D. Givord, J. Nogués, Nature 423 (2003) 850–853.
- [34] J. Leveneur, G.I.N. Waterhouse, J. Kennedy, J.B. Metson, D.R.G. Mitchell, J. Phys. Chem. C 115 (2011) 20978–20985.
- [35] D.K. Avasthi, J.C. Pivin, Curr. Sci. 98 (2010) 780–792.
- [36] C.W. Yuan, D.O. Yi, I.D. Sharp, S.J. Shin, C.Y. Liao, J. Guzman, J.W. Ager, E. E. Haller, D.C. Chrzan, Phys. Rev. Lett. 102 (2009), 146101.
- [37] D.J. Sprouster, R. Giulian, L.L. Araujo, P. Kluth, B. Johannessen, D.J. Cookson, G. J. Foran, M.C. Ridgway, J. Appl. Phys. 107 (2010), 014313.
- [38] D.J. Sprouster, M.C. Ridgway, Appl. Sci. (2012) 2.
- [39] R. Janisch, N.A. Spaldin, Phys. Rev. B 73 (2006), 035201.
- [40] R.I. Khaibullin, L.R. Tagirov, B.Z. Rameev, S.Z. Ibragimov, F. Yildiz, B. Akta, J. Phys. Cond. Mat. 16 (2004) L443–L449.

- [41] A. Numan, N. Alexei, Z. Hartmut, W. Kurt, B. Hans-Werner, S. Christoph, G. Şafak, B. Asif, K. Rustam, T. Lenar, J. Phys. D: Appl. Phys. 42 (2009), 115005.
- [42] B.-F. Ding, Chin. J. Chem. Phys. 24 (2011) 724–728.
- [43] O. Yildirim, S. Cornelius, A. Smekhova, G. Zykov, Gan, apos, E. A. shina, A. B. Granovsky, R. Hübner, C. Bähtz and K. Potzger, J. Appl. Phys., 2015, 117, 183901.
- [44] J.P. Biersack, L.G. Haggmark, Nucl. Instrum. Methods 174 (1980) 257-269.
- [45] R. Abrudan, F. Brüssing, R. Salikhov, J. Meermann, I. Radu, H. Ryll, F. Radu, H. Zabel, Rev. Sci. Instrum. 86 (2015), 063902.
- [46] T.-D. Doan, C. Fermon, P. Humbert and E. Leymarie., SimulReflec: Reflectivity Curve Simulations and Fitting, http://www-llb.cea.fr/prism/programs/ simulreflec/simulreflec.html).
- [47] J.Y. Kim, J.H. Park, B.G. Park, H.J. Noh, S.J. Oh, J.S. Yang, D.H. Kim, S.D. Bu, T. W. Noh, H.J. Lin, H.H. Hsieh, C.T. Chen, Phys. Rev. Lett. 90 (2003), 017401.
- [48] K.L. Livesey, S. Ruta, N.R. Anderson, D. Baldomir, R.W. Chantrell, D. Serantes, Sci. Rep. 8 (2018) 11166.
- [49] S.R. Shinde, S.B. Ogale, J.S. Higgins, H. Zheng, A.J. Millis, V.N. Kulkarni, R. Ramesh, R.L. Greene, T. Venkatesan, Phys. Rev. Lett. 92 (2004), 166601.

- [50] K. Mamiya, T. Koide, A. Fujimori, H. Tokano, H. Manaka, A. Tanaka, H. Toyosaki, T. Fukumura, M. Kawasaki, Appl. Phys. Lett. 89 (2006), 062506.
- [51] B. Liu, C. Piamonteze, M.U. Delgado-Jaime, R.-P. Wang, J. Heidler, J. Dreiser, R. Chopdekar, F. Nolting, F.M.F. de Groot, Phys. Rev. B 96 (2017), 054446.
- [52] H. Wang, C. Bryant, D.W. Randall, L.B. LaCroix, E.I. Solomon, M. LeGros, S. P. Cramer, J. Phys. Chem. B 102 (1998) 8347–8349.
- [53] S. J. Callori, T. Saerbeck, D. L. Cortie and K.-W. Lin, in Solid State Physics, ed. R. L. Stamps, Academic Press, 2020, vol. 71, pp. 73-116.
- [54] J. Bertinshaw, S. Bruck, D. Lott, H. Fritzsche, Y. Khaydukov, O. Soltwedel, T. Keller, E. Goering, P. Audehm, D.L. Cortie, W.D. Hutchison, Q.M. Ramasse, M. Arredondo, R. Maran, V. Nagarajan, F. Klose, C. Ulrich, Phys. Rev. B 90 (2014) 5.
- [55] D.L. Cortie, K.W. Lin, C. Shueh, H.F. Hsu, X.L. Wang, M. James, H. Fritzsche, S. Bruck, F. Klose, Phys. Rev. B 86 (2012) 10.
- [56] T.S. Krasienapibal, T. Fukumura, T. Hasegawa, Electronics 6 (2017) 23.
- [57] S.A. Chambers, T. Droubay, C.M. Wang, A.S. Lea, R.F.C. Farrow, L. Folks, V. Deline, S. Anders, Appl. Phys. Lett. 82 (2003) 1257–1259.